Received: 26 August 2019 | Revised: 27 April 2020 | Accepted: 27 April 2020

DOI: 10.1002/eco.2216

RESEARCH ARTICLE

WILEY

Spatial upscaling of CO_2 emissions from exposed river sediments of the Elbe River during an extreme drought

Ulf Mallast[1] | Maren Staniek[2] | Matthias Koschorreck[3]

[1]Department of Monitoring and Exploration Technologies, HelmholtzCentre for Environmental Research (UFZ), Leipzig, Germany

[2]Department Catchment Hydrology, HelmholtzCentre for Environmental Research (UFZ), Halle, Germany

[3]Department of Lake Research, HelmholtzCentre for Environmental Research (UFZ), Magdeburg, Germany

Correspondence
Ulf Mallast, Department of Monitoring and Exploration Technologies, HelmholtzCentre for Environmental Research (UFZ), Permoserstraße 15, 04318 Leipzig, Germany.
Email: ulf.mallast@ufz.de

Funding information
Modular Observation Solutions for Earth Systems (MOSES)

Abstract

Droughts lead to falling river water levels and consequently expose river sediments. It is well known that from these exposed aquatic sediments, CO_2 emits to the atmosphere, but upscaling of CO_2 measurements from discrete point measurements to an entire river system remains challenging. Naturally occurring heterogeneous processes must be accounted for to obtain an overall CO_2 flux and to assess its significance. We contribute to this challenge by incorporating a two stage scaling approach using in situ CO_2 fluxes and remote sensing data. First, by combining optical airborne data with closed chamber measurements at a representative model site during a first scaling stage, we derive land cover type specific CO_2 fluxes and identify distance to the water as the most suitable proxy for further upscaling. Second, we upscale derived spatial relations from the first scaling stage to the entire river system of the Elbe River using a satellite-based analysis. In this way, we derived area-weighted CO_2 emissions from exposed river sediments of 56.6 ± 64.8 tC day^{-1} (corrected distance proxy) and 52.9 ± 44.6 tC day^{-1} (land cover proxy), respectively, for 1 day during the 2018 extreme drought. Given the intensification of droughts in terms of length and reoccurrence frequency, this result not only highlights the importance of drought-induced exposition of river sediment as a source of atmospheric CO_2 but also underscores the ability to monitor CO_2 emissions over an entire river system on a regular basis using remote sensing.

KEYWORDS

carbon dioxide emission, chamber measurements, hydrological drought, Sentinel-2, upscaling

1 | INTRODUCTION

Droughts and related low water levels have a large impact on river ecosystems as they are major regulators of biogeochemical cycling in river floodplain systems (Humphries & Baldwin, 2003; Junk, Bayley, & Sparks, 1989; Lake, 2003). With an expected increased reoccurrence frequency in the context of climate change (Stocker et al., 2013) such as in the Mediterranean, large streams will face pronounced periods with low water level conditions and thus an exposition of river sediments, whereas small streams will be more frequently prone to desiccation (e.g., Steward, von Schiller, Tockner, Marshall, & Bunn, 2012). For the latter, drought effects on greenhouse gas (GHG) emissions are intensively studied (Looman, Maher, Pendall, Bass, & Santos, 2017). Much less is known about GHG emissions from exposed sediments in high-order rivers, where sediments are typically more fine grained and the effect of exchange with the groundwater and interstitial water is

probably less pronounced (Bolpagni, Laini, Mutti, Viaroli, & Bartoli, 2019).

Recent evidence points to increased emission of especially CO_2 into the atmosphere from these exposed sediments at low water levels (Gallo, Lohse, Ferlin, Meixner, & Brooks, 2014; Gómez-Gener et al., 2015; von Schiller et al., 2014). During droughts, these exposed sediment areas are maximized, and microbial activities are stimulated by wet–dry cycles (Weise et al., 2016). On a global scale, initial rough estimates have shown that these emissions are likely to be an important but yet overlooked source of atmospheric CO_2 (Marcé et al., 2018). Nevertheless, upscaling spatially heterogeneous processes to entire river systems remains a challenge (Duvert, Butman, Marx, Ribolzi, & Hutley, 2018).

Exposed sediments comprise a diversity of land cover being a complex mosaic of sand and mudflats with or without pioneering vegetation (Bolpagni, Folegot, Laini, & Bartoli, 2017). This intermediate scale heterogeneity prevents the use of spatially integrating methods such as eddy covariance to measure CO_2 emissions as the method requires a larger homogenous footprint area (Aubinet, Vesala, & Papale, 2012). The only available method to measure CO_2 emissions in these heterogeneous areas is discrete point measurements using closed chambers (e.g., Bolpagni et al., 2017; Lesmeister & Koschorreck, 2017). Chamber-based CO_2 measurements proved to vary between land cover and are affected by sediment texture, sediment organic matter, sediment moisture, sediment temperature and chlorophyll *a* (Gallo et al., 2014; Gómez-Gener et al., 2015). However, upscaling discrete point measurements to the entire system is mostly prevented by the lack of information on the sheer size of exposed river sediments and their land cover (Gómez-Gener et al., 2015). If representative flux data can be aligned and area-weighted with spatial information on land cover distribution and the size of exposed river sediments, the assessment of the large scale CO_2 emission significance would be enabled (Macklin, Maher, & Santos, 2014).

The combination of spatially continuous satellite and airborne-based remote sensing data with discrete point measurements of CO_2 flux is the most promising approach for large scale quantification. Among others, these data facilitated in the classification of community and habitat levels in order to derive landscape properties including their heterogeneity and to determine inundation patterns. Depending on the remote sensing platform, spatial coverage and spatial resolution varies between 10^1 and 10^3 m^2 and 1–500 m, respectively (Melack et al., 2004; Mertes, 2002).

Similar satellite-based studies upscaled in-situ GHG emissions to entire highorder river systems (Striegl, Dornblaser, McDonald, Rover, & Stets, 2012) or to wetlands (Melack et al., 2004). The disadvantage using solely satellite data concerns the scaling from discrete measurements to pixel sizes of more than 900 m^2. The scaling inevitably leads to large uncertainties as it neglects small-scale habitat heterogeneity with different land cover as well as governing flux processes.

The present study seeks to include small-scale heterogeneity by incorporating a two stage scaling approach. Whereas in-situ land cover specific CO_2 fluxes allow assessment of the specific role for the total CO_2 emission, optical airborne data help to identify governing spatial relations between CO_2 fluxes and land cover of exposed river sediments during a first scaling stage. The second scaling stage represents a satellite-based analysis that upscales derived spatial relations from the first scaling stage to an entire river system. As a test case, we use Germany's third largest river, the Elbe River, during the millennium drought in summer 2018, which experienced historically low water levels recorded at several gauging sites (BfG, 2019). Based on both scaling stages, we quantify the total CO_2 emission from exposed river sediments for 1 day for the entire Elbe River and provide an outlook for future research directions to reliably quantify CO_2 on a river scale on a weekly basis.

2 | MATERIALS AND METHODS

2.1 | Study site and millennium drought

The study encompasses the German section of the Elbe River (Figure 1), Germany's third largest river with a mean annual discharge of 554 m^3 s^{-1} at the gauge Magdeburg Strombrücke. Compared with other larger German rivers, the Elbe River is less channelized and characterized by a comparably large floodplain (Scholten et al., 2003). Seasonal water level fluctuations between 1.2 and 3.1 m as indicated by the standard deviation from the mean are shaping different habitat types including vegetation free sandflats as well as dense reed stands, pastures and floodplain forest (Scholz, 2005).

The year 2018 was the hottest year since the beginning of weather recording in Germany in 1881. Extremely low rainfall in spring and summer resulted in the lowest water level ever recorded in the Elbe River (BfG, 2019; see Figure 1). At Magdeburg Strombrücke, the water level dropped to 45 cm, which is 47 cm below the mean annual low water level (LHW, 2019). The river was not navigable between June and the end of the year. The extremely low water level exposed large areas of river sediments to the atmosphere. Due to the abnormally low streamflow with inadequate surface water resources for established water uses, we define the period of July 2018 as clear hydrological drought following recommendations by Mishra and Singh (2010).

To cover the entire German Elbe River system in its longitudinal profile between the Czech border (Elbe km 0) and close to the Weir Geesthacht (Elbe km 586 km), we use a satellite-based remote sensing approach. A representative model site near the city of Magdeburg complements the river scale at which fieldwork was conducted. The model site consists of exposed river sediments of two habitats (sandflat in a side arm of the main stream and a typical groyne field in the main channel; Figure 2) with different land cover. This area is exposed as soon as the water level falls below its mean level of 189 cm. During the 2018 extreme drought, this condition along with a stagnant or falling water level occurred for a total of 117 days (Figure 1).

On 25 July 2018, we conducted CO_2 flux measurements at 28 locations covering different land cover types such as dry grass

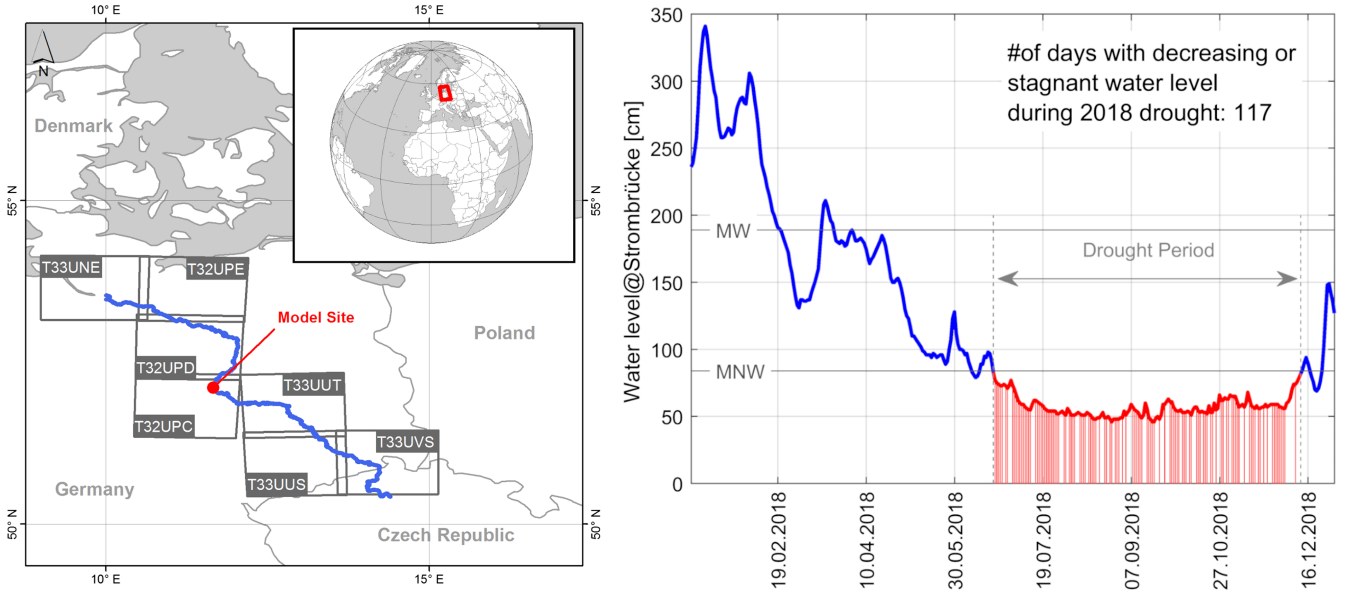

FIGURE 1 Overview on location of the Elbe (blue line) and the model site, along with spatial coverage of applied Sentinel-2 satellite scenes (left); Elbe water level during the year 2018 showing the extreme drought effect on the water level and the number of days during which the water level was stagnant or falling (red vertical lines). Note that MW indicates the mean water level and MNW the mean annual low water level given by the Federal Waterways and Shipping Administration

(five locations), grass (three locations), reed (two locations) and bare sediment (18 locations). The latter encompasses visually observed sediment colour differences with presumably different CO_2 fluxes. We therefore divided this land cover into three subclasses: bright (three locations), brown (12 locations) and dark (three locations) sediment (Figure S1). Each location was surveyed with a differential GPS system resulting in ±3 cm spatial accuracy.

2.2 | CO_2 flux measurements

The CO_2 fluxes were measured with static chambers connected to gas analysers. To map unvegetated sites, we used a commercially available system (Soil Respiration Chamber SRC1 + EGM, PPSystems, USA) with only dark measurement (Pumpanen et al., 2004). At vegetated sites, we used a custom made circular transparent chamber (diameter 23 cm; Figure S1) applying a fourfold to sixfold replication. The chamber was equipped with a pressure vent (Hutchinson & Mosier, 1981) and installed on soil collars made from standard PVC tubes. Depending on vegetation height, we used two different chamber heights (15 or 50 cm). The concentration of CO_2 in the chamber was continuously monitored by a portable GHG analyser (microportable GHG analyser, LosGatos Research, USA). Previous tests had shown that our system gave reliable flux data without using preinstalled collars (Lesmeister & Koschorreck, 2017) and that the pump of the gas analyser created enough air mixing in the chamber that we could do without a fan (Koschorreck, unpublished).

Flux measurements with the commercial system lasted 2 min or until the CO_2 change exceeded 50 ppm—depending on which of these two criteria was met first. At vegetated sites, we used a transparent chamber covering the herbaceous vegetation (<15 cm height) or reed (about 50 cm height). Because the volume to area ratio of these chambers was higher than that of the commercially available system, we increased the measurement time. Measurements with the transparent chamber were performed over 5 min (light flux) after which the chamber was shaded by a dark foil and the measurement continued for another 5 min (dark flux). Previous repeated light–dark–light measurements had shown that it was not necessary to vent the chamber between light and dark measurements. Temperature in the chamber was recorded by a wireless thermometer. Temperature increase in the chamber during measurements never exceeded 2.5°C. Fluxes were calculated from the linear increase of the gases partial pressure over time. The CO_2 flux was calculated according to Equation 1

$$F_{CO_2} = \left(\frac{dpCO_2}{dt}\right)\left(\frac{V}{RTS}\right), \quad (1)$$

where F_{CO_2} = CO_2 flux (mmol m^{-2} day^{-1}), $dpCO_2/dt$ = slope of the change in pCO_2 with time (µatm day^{-1}), V = volume of the chamber (m^3), S = surface area covered by the chamber (m^2), T = air temperature (K) and RTS = ideal gas constant = 8.314 (L atm K^{-1} mol^{-1}). To calculate mean daily CO_2 fluxes from vegetated sites, we calculated the day length weighted mean of light and dark fluxes considering a light period of 13.5 h day^{-1}.

To determine the significance of CO_2 flux differences among land cover types (see Section 2.4), we applied an ANOVA-based multiple comparison analysis using the least significance difference procedure using Matlab 2019b.

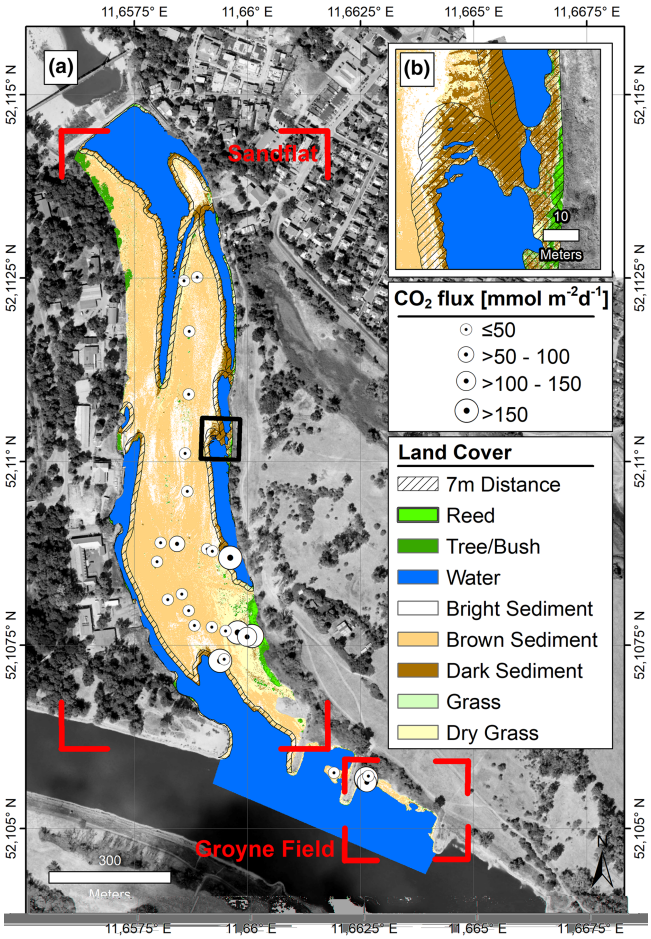

FIGURE 2 Result of the land cover classification for the model site of the study area and mean CO_2 value of each sample site (a) with a subset on a representative area showing the detailed land cover class distribution (b)

2.3 | Sediment measurements

Sediment measurements conducted at the abovementioned 28 sample sites focus on sediment water content, sediment temperature and grain size distribution. Measurements were repeated three times per sample site and then averaged.

Sediment water content and temperature were obtained at depths of approximately 5 cm using three replicate measurements each. Volumetric water content θ (m^3/m^3) was measured using a portable TDR100 time domain reflectometer (TDR; Campbell Scientific, Logan, UT) with a custommade threerod probe. Prior to the campaign, the TDR probe was calibrated for water content estimation with measurements in water and air. Using the Complex Refractive Index Model formula according to Roth, Schulin, Flühler, and Attinger (1990), we calculated the volumetric water content with an accuracy of ±0.02 m^3/m^3. Sediment temperature was measured with a DT300 handheld LCDthermometer (Voltcraft, Hirschau, Germany). Measurement accuracy is in the range of ±1°C in 3 to 6 cm depth.

Grain size distribution was determined through grab samples (~150 g) from a depth of 0–20 cm. Each sample was dried and manually sieved using mesh widths of 2, 1, 0.5, 0.25, 0.125, 0.063 and 0.032 mm to differentiate between gravel, sand, silt and clay fractions. Subsequently, the average of each fraction was calculated to obtain a representative value for each fraction.

2.4 | Remote sensing

We used optical airborne data during the first scaling stage to classify land cover of the exposed riverbed and to eventually identify governing spatial relations on a local scale. The core of the second scaling stage represents a satellite-based analysis that quantifies the total exposed riverbed area. With the exposed riverbed area, we were in the position to upscale derived spatial relations from the first stage's localscale results onto the German Elbe River scale. Both airborne and satelliteborne data, each with specific spectral and spatial characteristics and specific processing steps, are described hereafter.

2.4.1 | Airborne data and ground control data

To obtain airborne data, we used a Gyrocopter Cavalon D-MHSA as platform, an inertial measuring unit iMAR IMUFSAS in combination with the AeroDiDOS direct orientation system and differential GPS to obtain position and orientation angles at an accuracy of 0.02m RMS and height accuracy of 0.05 m after postprocessing. The applied AC8 RGBcamera system is essentially a Nikon D800e fullframe digital camera (focal length 55 mm/FPA 7360 × 4912) that was modified for use in a gyrocopter (Bannehr, Kirschke, Koppers, & Ulrich, 2015). Information of position (Lat, Lon and flight altitude), orientation angle (yaw, pitch and roll) and time stamp of each image was stored externally and later transferred to the image *exif* information of each image. The flight took place on 27 July 2018 between 13:42 and 15:00 local time (LT) at an altitude of ~610 m above ground level. During the time weather was partly cloudy with wind speeds of 1.7 m s^{-1}. With an along-track and across-track overlap of 50%, a total of 441 images were recorded that cover an area of ~5 km^2. To georeference image data, we distributed nine ground control points (GCPs) whose position was determined using a differential GPS with an overall accuracy of ±3 cm.

Data processing

The processing of recorded RGB images consisted of two consecutive steps. First, using a Structure from Motion approach, we applied the commercial software package Agisoft PhotoScan Professional version 1.4.2 to create an orthomosaic for the covered area using the image *exif* information and GCPs as ground reference. All images were aligned setting the accuracy settings to high and preselection based on GPS coordinates. Subsequently, we calculated the sparse point cloud, deleted outliers and reconstructed the detailed geometry (bundle adjustment) using a dense point cloud (reconstruction parameter:

surface type—height field; quality—high; depth filtering—mild). Based on the detailed geometry result, we identified the GCPs and used them to finetune the bundle adjustment that leads to the dense point cloud. The resulting digital orthomosaic (DOM) and digital surface model (DSM) were exported with a ground sampling distance of 13 cm with a RMSE of 20 cm (x), 23 cm (y) and 18 cm (z). As a final step, we reduced the total covered area of DOM and DSM to the area of interest, which we define as the area covered by water at Elbe mean water level.

Second, based on the spatially reduced DOM, we performed a maximum likelihood classification (MLC) to extract relevant land cover classes using ArcMap 10.7. These classes included water, bright sediment, brown sediment, dark sediment, grass, dry grass, reed and bush/tree. Due to the less complex nature of the input data, we defined three to 12 training samples per class based on our in-situ 28 sampling locations (each training sample contains several pixels) to discriminate between classes as suggested by Van Niel, McVicar, and Datt (2005). Training samples for classes that were not covered by in situ measurements such as water and bushes/trees were taken by dGPS measurements during the same day. All training data were input for the MLC process using equal weights for all classes. We validated our result with 50 points that were randomly distributed over the entire area. The number of validation points per class is based on the areal share of each class on the overall classification (Figure S2).

For each in situ sampling point, we assigned the respective land cover class, the elevation using the DSM and the Euclidean distance to water as spatial information. The latter was calculated using the water class from the MLC. In turn, we calculate the area-weighted CO_2 flux for each of the land cover/distance classes by averaging the CO_2 fluxes per class and multiplying it with the covered area per class.

2.4.2 | Satellite data

In order to determine the area of the exposed riverbed during the drought for the entire Elbe River, we used Sentinel-2 Level 1C data, which were downloaded from https://glovis.usgs.gov. These data are georeferenced, radiometrically corrected, top of atmosphere (TOA) reflectance values with a subpixel multi-spectral and multi-date registration (Drusch et al., 2012). Relevant scenes were selected based on two criteria: First, recording dates should reflect a point in time with an Elbe River mean water level (normal situation) and an Elbe River minimum-water level (drought situation), to be able to evaluate the amount of exposed river sediment during a drought. Second, the Elbe River should be only minimally covered by clouds or cloud free. Accounting for both criteria, the resulting satellite scenes along with orbits and tiles to cover the entire German part of the Elbe River is listed in Table S1. Due to cloud contamination, however, we could not process 50 km of the river between river km 260–280 and 360–380, which corresponds to 8% of the entire German Elbe River system.

Data processing

Each scene was automatically processed as follows using Matlab 2018a: A manually digitized vector file of the Elbe River was converted into a binary raster (river pixel = 1/background pixel = 0) format resembling the same extent and spatial resolution of the input Sentinel-2 scene. This binary Elbe River raster was morphologically dilated by 100 pixels to create a mask (hereafter Elbe mask) that spatially comprises the Elbe and its close proximity (500 m to each riverside). In a second step, the Normalized Difference Water Index (hereafter denoted as NDWI) after McFeeters (1996) was calculated for each Sentinel-2 scene using band 3 (TOA reflectance of the green fraction of the electromagnetic spectrum) and band 8 (TOA reflectance of the nearinfrared fraction) enabling us to differentiate between water and land (Du et al., 2016). After calculating NDWI, we applied the Elbe River mask and extracted only those NDWI values of land and water that are within the mask. To segment land and water respectively, we use the classical Otsu method (Otsu, 1979) based on grey-level histograms of NDWI values. As these values resemble a bimodal distribution, the optimal threshold is obtained by maximizing the between-class variance of both classes within the bimodal distribution (Otsu, 1979). The subsequent result shows a binary raster where ones represent water areas (objects), whereas zeros are land. To discriminate objects between unwanted water areas such as ponds, unconnected oxbows and the Elbe River, we used the previously created vector file. In the event that both were located at the same geoposition, the object was kept while remaining ones were deleted. With one object (Elbe River) remaining, we vectorized it (hereafter denoted as Elbe vector) and corrected for parts connected to the Elbe but irrelevant such as confluences. The final step consisted of merging the different Elbe vector files resulting from each Sentinel-2 scene for the normal and drought situation. Both vector files (drought and normal situation) were subsequently divided in 10 km segments, and for each of these segments, the water area was calculated.

3 | RESULTS AND DISCUSSION

3.1 | CO_2 flux at model site

CO_2 emissions from the model site showed considerable spatial heterogeneity. Dark fluxes (sediment respiration) ranged from −7 to 958 mmol CO_2 m^{-2} day^{-1} with a mean CO_2 flux of 150 ± 201 mmol m^{-2} day^{-1}. Yet CO_2 emission differences between land cover types are only significant for classes brown sediment/grass and brown sediment/reed with $p = 0.002$ and $p = 0.060$, respectively. All remaining comparisons were no significant with p values between 0.45 and 0.97.

Highest emissions were observed at vegetated sites and dark sediment but even bare sand classified as 'bright' and 'brown' sediment emitted substantial amounts of CO_2 (Table 1). Two flux measurements (one for brown and one for bright sediment) indicate small negative fluxes (CO_2 uptake), which may be explained by

TABLE 1 CO_2 fluxes of different land cover measured on 25 July 2018 by static chamber (mean ± SD, range in brackets)

Land cover type	Area (m^2)	(%)	CO_2 flux: Dark (mmol m^{-2} day^{-1})	CO_2 flux: Light	CO_2 flux: Daily	Vol. water content (Vol%)	Sediment temperature (°C)	Distance to water (m)	Elevation (m)
Bright sediment	15,560	14	21 ± 32 (−6–56)	ND	21 ± 32 (−6–56)	0.9 ± 0.6 (0.2–1.3)	37.8 ± 0.0	48.4 ± 17.5 (36.9–68.6)	40.6 ± 0.2 (40.3–40.7)
Brown sediment	68,871	61	19 ± 12 (−7–35)	ND	19 ± 12 (−7–35)	3.6 ± 10.1 (0–35.5)	37.7 ± 1.7 (33.8–40.6)	39.5 ± 17.8 (7.0–64.0)	40.0 ± 0.3 (39.5–40.4)
Dark sediment	7,771	7	136 ± 56 (55–197)	ND	136 ± 56 (55–197)	30.8 ± 5.3 (22.1–35.8)	36.2 ± 2.3 (33.1–38.7)	1.9 ± 2.7 (0.5–6.7)	39.2 ± 0.2 (39.0–39.4)
Dry grass	18,868	16	73 ± 84 (5–200)	ND	73 ± 84 (5–200)	0.3 ± 0.3 (0–0.8)	38.1 ± 1.9 (35.3–39.6)	38.2 ± 21.2 (8.3–58.8)	39.8 ± 0.2 (39.6–40.0)
Grass	1,003	1	115 ± 100 (3–288)	−31 ± 49 (−109–11)	90 ± 112 (−39–288)	3.4 ± 2.7 (0.5–7.2)	36.3 ± 1.1 (35.3–38.2)	10.3 ± 6.5 (3.5–17.3)	39.6 ± 0.1 (39.5–39.7)
Reed	1,052	1	332 ± 338 (3–958)	5 ± 167 (−139–217)	147 ± 148 (3–438)	1.0 ± 1.2 (0.0–3.2)	38.2 ± 1.6 (36.5–40.1)	39.5 ± 28.6 (9.6–64.4)	40.0 ± 0.2 (39.8–40.2)
≤7 m	23,172	20	197 ± 64 (101–261)		197 ± 64 (101–261)	23.8 ± 15.0 (4.9–36.9)	36.7 ± 2.3 (33.1–38.7)	3.6 ± 3.0 (0.5–6.7)	39.3 ± 0.3 (39.0–39.7)
>7 m	89,954	80	42 ± 61 (−7–236)		42 ± 61 (−7–236)	5.3 ± 7.6 (0.1–39.8)	37.7 ± 1.5 (33.8–40.6)	39.2 ± 19.2 (7.0–68.6)	40.0 ± 0.4 (39.5–40.7)

Note: For vegetated sites, daily CO_2 fluxes were calculated from day length (light period 15.3 h day^{-1}) weighted light and dark fluxes, for non-vegetated sites the daily value corresponds to the dark value. ND = not determined. Note that for areal share calculation, the classes Tree/Bush and Water shown in Figure 2 are not considered since we focus on exposed sediments only.

chemical weathering (Light, Catalán, Giralt, & Marcé, 2019). The general CO_2 flux picture displays the highest fluxes for land cover types such as dark sediment, reed and grass, which cover only 9% of the total area, whereas land cover types with lower fluxes cover 91% of the study area (Figure 2).

As expected, CO_2 fluxes at vegetated sites were lower or even negative in the light. However, on a daily scale, even vegetated sites were net CO_2 emitters, indicating that primary production was compensated by respiration and/or CO_2 input from sediment or groundwater.

3.2 | CO_2 parametrization

Table 1 indicates CO_2 flux dependence on land cover and thus is in line with Bolpagni et al. (2019). CO_2 fluxes differed depending on prevailing conditions such as sediment temperature, water content, texture, elevation and distance to water (Figure 3). Despite the fact that CO_2 flux had been shown to relate to sediment temperature (Martinsen, Kragh, & SandJensen, 2019), higher and lower fluxes occurred over the entire sediment temperature range with no clear trend for any of the land cover classes (Figure 3a), which agrees with results of Gallo et al. (2014). However, the temperature range covered by our data was rather small, which hampers an in-depth analysis of temperature dependence.

As for the sediment water content, although Gómez-Gener et al. (2015) report a negative correlation between water content and CO_2 flux, we cannot identify any clear trend between the two. Nonetheless, land cover classes tend to cluster (Figure 3b). The classes dark sediment and grass/reed reflect higher CO_2 fluxes with 136 and 147 mmol m^{-2} day^{-1}, respectively, but different water content values of ~31 Vol% and ~11 Vol%. Bright/brown sediment shows the lowest CO_2 fluxes with less than 21 mmol m^{-2} day^{-1} and water content of less than 3.6 Vol%. Thus, in terms of spatial CO_2 flux distribution, both dark sediment and grass/reed classes seem to be of higher importance, but water content alone does not serve as proxy.

Grain size likewise had no influence on CO_2 fluxes (Figure 3c) and thus underscores the dependence of CO_2 to grain size gradients (Gómez-Gener et al., 2016). Only one sample had a silt content of more than 6 M%, all remaining ones range between 0 and 1.4 M%, independent of land cover class. The uniformity of grain size distribution is likely to be caused by uniform sedimentation behaviour in the study area as it remains a connected oxbow with a low flow regime.

Elevation on the contrary, seems to have a slight indicator value as proxy for CO_2 flux. Higher fluxes scattered in the lower range of elevations (39–40 m). Lower CO_2 fluxes plot in elevated regions of 39.5–40.7 m (Figure 3d) with an overlapping area of 39.5–40 m in which higher and lower CO_2 fluxes occur in parallel. Striking in this context is that only vegetated samples such as reed, grass and dry grass scatter in the overlap area. The reason is likely to be associated with the methodical procedure for retrieving elevation. The applied photogrammetry approach is based on optical data. It produces a surface model rather than an elevation model, which includes plant heights (Watanabe & Kawahara, 2016). As the plant heights varied

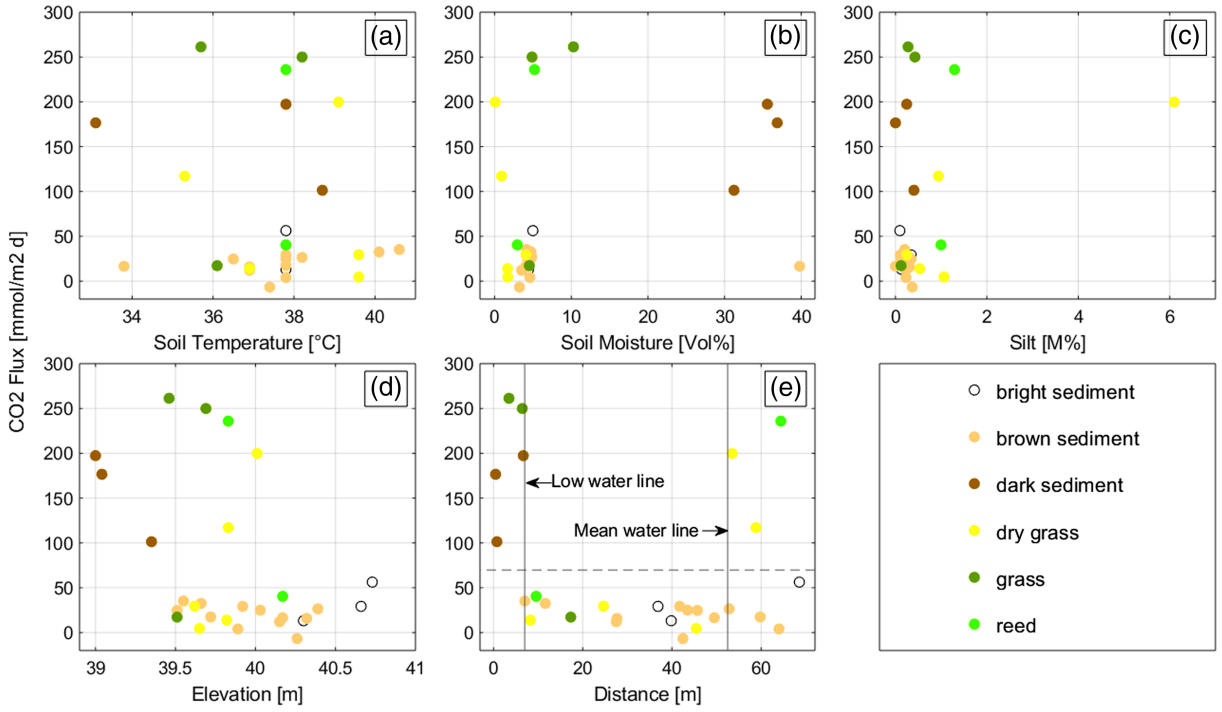

FIGURE 3 Dependence of CO_2 flux to prevailing spatial conditions such as soil temperature, soil moisture, silt, elevation and distance to water at the model site. Note: land cover classes are colour coded. Mean and low water lines in (e) indicate measuring locations with higher CO_2 values likely to be affected by low water level and higher water level. The horizontal line in the same panel indicates the mean CO_2 value for all sample sites

between 10 and 50 cm, the actual surface elevation at these vegetation covered sites is lower at an elevation range of less than 39.5 m. With the correction, the elevation would correspond to the elevations showing high CO_2 fluxes. Different techniques such as PRF LIDAR (Rogers, Parrish, Ward, & Burdick, 2018) or L-band radar (Hensley et al., 2015) offer the possibility to reduce the effect of plants on elevation models due to their technical nature and may be preferable over optical data. Once retrieved, derivable geomorphology that determines physical characteristics of the exposed riverbed such as water content and organic matter deposition may serve as an appropriate proxy for CO_2 flux (Arce et al., 2019).

However, as retrieving true elevation for the present case was hampered, the Euclidean distance of CO_2 measurements to water is more promising as proxy as Figure 3e shows. Within a distance of 7 m CO_2 fluxes were highest with values of 101–261 mmol m^{-2} day^{-1} (median of 197 mmol m^{-2} day^{-1}). With distances of more than 7 to 52m fluxes dropped below −7–40 mmol m^{-2} day^{-1} (median of 17 mmol m^{-2} day^{-1}). Only at distances of more than 52 m elevated CO_2 fluxes of up to 4–235 mmol m^{-2} day^{-1} (median of 56 mmol m^{-2} day^{-1}) reoccured. We argue that both areas with elevated CO_2 fluxes represent different water levels. The more distant area represents the mean water line for our study area along with well-developed reed stands and higher grass. Higher CO_2 fluxes in this area may be attributed to root respiration at vegetated sites that has been shown to account for about half of the CO_2 production in soils (Hanson, Edwards, Garten, & Andrews, 2000). Higher CO_2 fluxes in this area may also be attributed to the availability of organic matter that is trapped in the rather stable environment (Bolpagni et al., 2017), along which new biomass (mostly reed) can develop. Organic matter is then decomposed by microbial activity causing higher CO_2 fluxes (Gallo et al., 2014).

The closer area within 7 m in which we observed higher CO_2 fluxes is represented by two land cover classes: grass and dark sediment. Figure 3b already indicates that dark sediment was wetter than the other sites. At the time of our study, grass, which is pioneering and ephemeral, did not act as a sink on a daily basis as reported in Bolpagni et al. (2017). Obviously, photosynthesis was compensated by CO_2 producing processes like heterotrophic activity and/or CO_2 input from groundwater. Most probably, the plants were already withering due to the drought and the extreme heat.

Concluding, there is an obvious spatial dependence between higher CO_2 flux and distance to water which is in line with observations of Jin et al. (2016) and Bolpagni et al. (2017). We hypothesize the mechanism behind this to be the higher groundwater level compared with the river water level. Compared with the river system, the response of the groundwater system to drought is delayed (Peters, Bier, Van Lanen, & Torfs, 2006; Tweed, Leblanc, & Cartwright, 2009). The delay results in higher groundwater level than river water level and thus in flow gradients towards the river. With flow gradients towards the river, the exposed riverbed area between groundwater and river water levels is constantly rewetted through discharging groundwater. Upon reaching the sediment-atmosphere interface, CO_2 dissolved in groundwater degasses. This process leads to higher CO_2 fluxes, a fact that is also reported by Macklin et al. (2014) for estuarine canal estate waters that tap surrounding aquifers thereby artificially creating groundwater discharge hotspots. Nevertheless, besides purely physical mobilization of groundwater-borne CO_2, it is also likely that groundwater-induced rewetting stimulates microbial respiration in the sediment, which may additionally contribute to CO_2 fluxes as described in Borken, Davidson, Savage, Gaudinski, and Trumbore (2003).

The land cover class dark sediment supports the logical chain in our hypothesis (Figure 3b,d). This class exhibits lower elevations (less than 39.4 m), corresponds to higher moisture states (more than 30 Vol%) and to higher CO_2 emissions (101–200 mmol m^{-2} day^{-1}). Further classes with higher CO_2 fluxes such as grass, dry grass and reed reflect only slightly higher moisture states (4.8–10 Vol%) compared with all other classes with less than 4 Vol%. The slightly higher moisture states can be explained with the increased need for pioneering plants for water during drought. All available water in the upper centimetre will be used for plant uptake which results in reduced sediment moisture. Elevations for these classes as given in Figure 3 may be corrected to values less than 39.5 m (see prior explanation) and would thus be in line with characteristics of the dark sediment class. However, all are within a distance of less than 7 m to water and thus support our hypothesis of higher groundwater tables to be the likely cause for higher CO_2 fluxes induced by a delayed response of the groundwater system to droughts. Hence, for the present case, the 7 m distance to water is a justified proxy for higher CO_2 fluxes and elemental for both subsequent upscaling stages as described below.

3.3 | Upscaling of CO_2 fluxes from point to local scale (first scaling stage)

As comparison with the rather simple and possibly generalizing distance proxy, we additionally used the land cover data as obtained from the MLC as second proxy to obtain a further area-weighted CO_2 flux. Using the resulting land cover areas of the MLC and the distance proxy, we obtained the area-weighted CO_2 flux for the entire model area. Due to level of land cover detail, we assume the results to approach the actual overall flux conditions.

Figure 2 shows the results of the MLC whereas Table 2 presents the areal share of each land cover class and associated total daily CO_2 fluxes. Following the first upscaling approach (land cover proxy), we observed that due to the areal shares, the highest area-weighted CO_2 fluxes occurred in the land cover of dry grass and brown sediment with 0.06 tC day^{-1} although both exhibited a medium to low discrete in-situ flux magnitude (see Table 1). On the contrary, the class dark sediment covered a significantly smaller area, the area-weighted CO_2 flux amounted to a similar value of 0.05 ± 0.02 tC day^{-1}. All remaining classes including reed and grass with evidently higher discrete in-situ flux magnitudes had significantly lower area-weighted CO_2 fluxes with 0.1 ± 0.2 tC day^{-1}, respectively. Thus, the detailed land cover classification underscores the fact that land cover representing classes

TABLE 2 Comparison of area-weighted CO_2 fluxes using different scaling approaches presented within this study (mean ± SD)

Scaling approach	Land cover class	Area (m^2)	Area (%)	Daily CO_2 flux ($tC\ day^{-1}$)	Sum of all daily CO_2 fluxes ($tC\ day^{-1}$)
Detailed land cover proxy	Bright sediment	15,560	14	**0.01 ± 0.02**	**0.20 ± 0.17**
	Brown sediment	68,871	61	**0.06 ± 0.04**	
	Dark sediment	7,771	7	**0.05 ± 0.02**	
	Dry grass	18,868	16	**0.06 ± 0.07**	
	Grass	1,003	1	**0.01 ± 0.01**	
	Reed	1,052	1	**0.01 ± 0.01**	
Distance proxy	≤7 m	23,172	20	**0.20 ± 0.07**	**0.37 ± 0.30**
	>7 m	89,954	80	**0.17 ± 0.24**	
Distance proxy (heterogeneity corrected)[a]	≤7 m	23,172	20	**0.05 ± 0.02**	**0.22 ± 0.24**
	>7 m	89,954	80	**0.17 ± 0.24**	

Note: For the scaling approach 'distance proxy with heterogeneity', the derived factor of 0.27 to account for heterogeneity was applied to the class <7 m only.

[a]Heterogeneity corrected refers to the elaborated percentile area weights of 27% of the class 'dark sediment' included in the <7 m distance class (see Section 3.3).

with active vegetation was less important considering the overall area-weighted CO_2 flux of 0.20 ± 0.17 tC day^{-1}. On the contrary, the classes dark/brown sediment and dry grass contribute 83% to the overall weighted CO_2 flux of 0.20 ± 0.17 tC day^{-1}. Although this general picture remains valid, the classification uncertainty for the classes dry grass and grass (Figure S2) introduce a certain degree of uncertainty for the CO_2 flux of both classes.

Using the distance proxy as upscaling approach results in a higher overall area-weighted CO_2 flux of 0.37 ± 0.30 tC day^{-1} (Table 2) suggesting a CO_2 flux overestimation compared with the obtained values using the detailed land cover proxy. The difference can be attributed to the aquifer heterogeneity that is also mentioned in Duvert et al. (2018). Aquifer heterogeneity results in non-homogenous groundwater discharge over the entire 7 m distance area. Instead, discharge can be assumed localized. Figure 2b supports the patchiness indicating that the class dark sediment as indicator for moister, and thus groundwater discharge areas with higher CO_2 fluxes, is one contributor among others over the 7 m distance. In fact, the class dark sediment accounted for only 27% of the total of less than 7 m area. If we account for the lower areal share of 27% thereby including aquifer heterogeneity, we obtain an area-weighted overall CO_2 flux of 0.22 ± 0.24 tC day^{-1}, which matches remarkably the area-weighted overall flux of the detailed land cover scaling approach (Table 2).

Since detailed land cover data may not be generally available at other study sites or over large spatial scales and water areas can be easily extractable using different approaches and platforms even over large spatial scales (Ghahremani & Bondarev, 2017; Gleason et al., 2015; Kaplan & Avdan, 2017), we argue that the corrected distance proxy is a reasonable approach to upscale discrete in-situ CO_2 measurements. However, as hydrogeological and sedimentological conditions may change along a river as indicated by Duvert et al. (2018), distance dependency may be site specific and thus may vary to the 7 m distance value elaborated in the present study or even over time. Future in-situ measurements should therefore focus on a validation and possibly better representation of CO_2 measurements on exposed river sediment close to water.

3.4 | Upscaling of CO_2 fluxes from local to Elbe scale (second scaling stage)

The second scaling stage relies on the knowledge of the area of exposed river sediments during drought periods. For the German Elbe, the 2018 drought exposed 28.62 km^2 of river sediments compared with the water area covered during mean water level. Given a total Elbe water area of 106.4 km^2 during mean level conditions as retrieved from the satellite analysis, the percentage water area reduction during the drought 2018 amounts to 26.9% varying between 2% and 40% throughout the longitudinal profile of the Elbe River (Figure 4a). Although the relative values would not change, the absolute areas of exposed river sediments may increase by ~10% accounting for the missing area that could not be processed due to cloud contamination.

The variation and thus the amount of exposed river sediments is mainly governed by the river width and the number of groyne fields. The more groyne fields exist and the wider the river, the higher the variation and area of exposed river sediments. Both steadily increase over the entire longitudinal profile of the Elbe River and reach their maximum between river km 400 and 540 (Figure 4a; IKSE, 2005). At this maximum the exposed river sediment area amounts to ~1 km^2 per 10 km river segment during drought conditions, whereas upstream, it varied between 0.2–0.6 km^2 (Figure 4b). Beyond km 540,

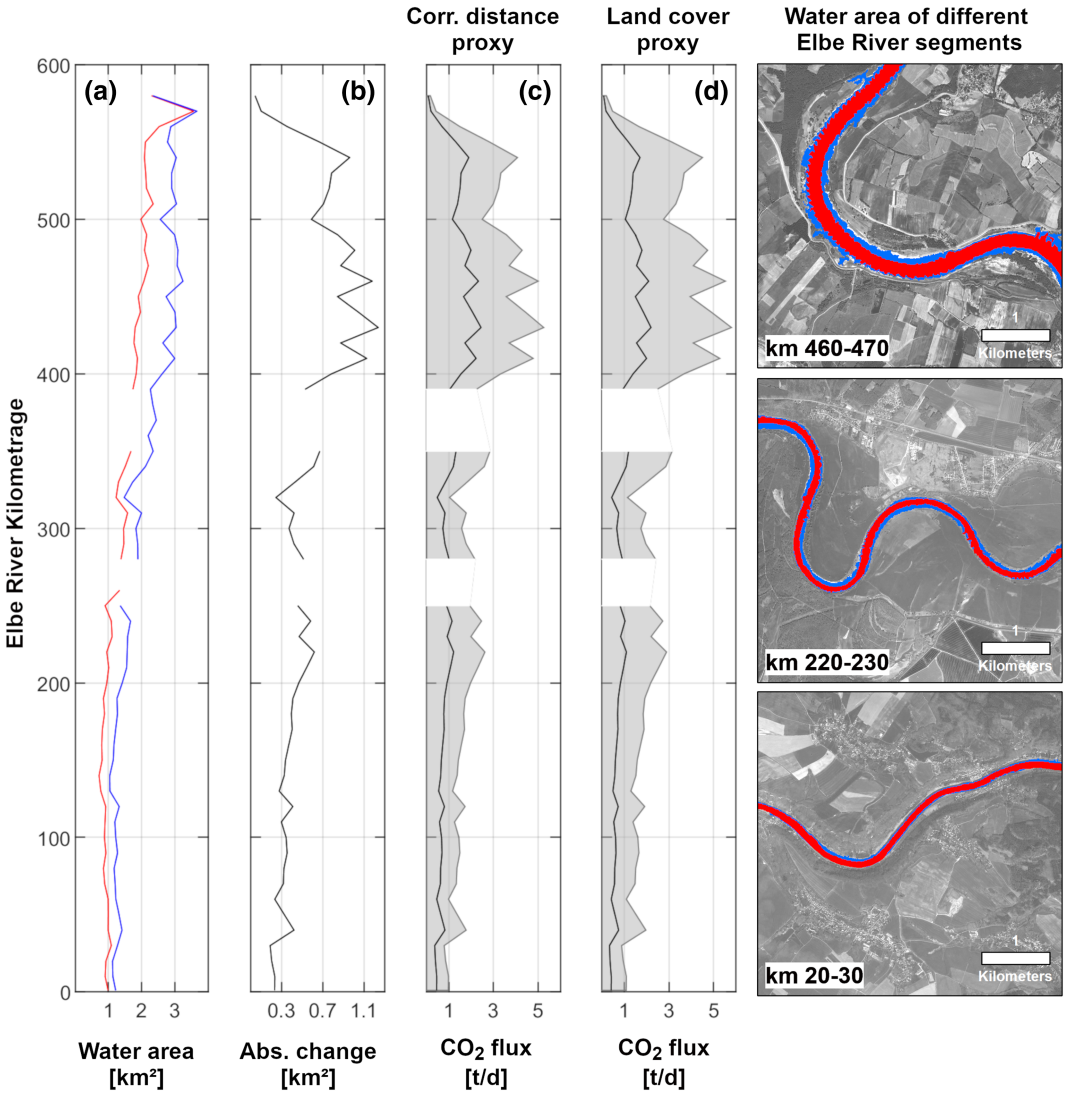

FIGURE 4 Elbe water area for 10 km segments along the entire longitudinal profile is shown during drought conditions in October 2018 (red curve) and during mean level conditions (blue curve) in (a); the absolute area of so exposed river sediments between drought and mean level conditions is shown in (b); calculated CO_2 flux using the derived distance proxy is shown in (c); calculated CO_2 flux using the detailed land cover is shown in (d). Different exemplary Elbe river segments illustrate the water area between mean level conditions (blue) and drought conditions (red). The difference of both results in the exposed river sediment area

the Elbe is influenced by the weir at Geesthacht, which reduces the exposed area to a minimum of 0.04 km^2 (IKSE, 2005).

Taking the deduced area of exposed river sediments of the entire Elbe as a basis and applying the above elaborated percentile area weights of the heterogeneity-corrected distance proxy and the detailed land cover proxy to upscale CO_2 flux measurement for each of the 10 km segments results in the values shown in Figure 4c,d. Analogous to the exposed river sediment area, CO_2 fluxes increased steadily until km 400 reaching values of 2.5–3.0 tC day^{-1} for both upscaling proxies. Between km 400 and 540, fluxes of both increased to values more than 5 tC day^{-1}. The overall flux for the heterogeneity-corrected distance proxy results in a total 56.6 ± 64.8 tC day^{-1} of CO_2 emissions, whereas the second more detailed upscaling approach (land cover proxy) provides a CO_2 flux of 52.9 ± 44.6 tC day^{-1} (Table 3).

Both upscaling approaches assume a spatiotemporal continuity in terms of areal share, land cover and an equally dissolved amount of CO_2 in groundwater alongside the entire river system. Considering the sediment variability over the entire longitudinal profile of a river system, a gradual increase of fine material towards downstream sections is likely to be reflected in the sediment banks, which may cause better conditions for pioneering plants and which does affect total CO_2 emissions. Pioneering plants require time to develop and to spread on exposed river sediment areas but contribute substantially to overall CO_2 flux through root respiration as shown for grass and reed. Typically, root respiration contributes about 50% to total soil respiration in vegetated soils, but values can go up to more than 90% (Hanson et al., 2000). Although it could not be investigated during the present study, microbial activity is likely to contribute to overall CO_2 flux as well (Gallo et al., 2014). The contribution may be more

TABLE 3 Daily CO_2 fluxes for the entire Elbe River at the example of two upscaling approaches (detailed land cover and distance proxy of 7 m)

Scaling approach	Land cover class	Area (km^2)	Daily CO_2 flux for entire Elbe ($tC\ day^{-1}$)	Sum of daily CO_2 fluxes per scaling approach ($tC\ day^{-1}$)
Detailed land cover	Bright sediment	3.9	**3.7 ± 5.5**	**52.9 ± 44.6**
	Brown sediment	17.4	**14.9 ± 9.3**	
	Dark sediment	2.0	**11.7 ± 4.8**	
	Dry grass	4.8	**15.3 ± 17.6**	
	Grass	0.3	**3,4 ± 3.4**	
	Reed	0.3	**3.9 ± 4.0**	
Distance proxy	≤7 m	5.9	**50.9 ± 16.6**	**94.0 ± 77.0**
	>7 m	22.8	**43.1 ± 60.4**	
Distance proxy (heterogeneity corrected)[a]	≤7 m	5.9	**13.5 ± 4.4**	**56.62 ± 64.8**
	>7 m	22.8	**43.1 ± 60.4**	

Note: The basis for the area calculation is taken from exposed river sediment area of 28.62 km^2 for the 2018 drought and the areal share dervied from the previous upscaling stage.

[a]Heterogeneity corrected refers to the elaborated percentile area weights of 27% of the class 'dark sediment' included in the <7 m distance class (see Section 3.3).

pronounced at the groundwater rewetted fringe along the river or at vegetated sites of the newly exposed areas. In the latter case, vegetation may act as a trap for organic matter that later becomes decomposed microbial material leading to higher CO_2 fluxes.

Apart from spatial heterogeneities over the largescale river system, it is also likely that temporal fluctuations exist. Marcé et al. (2018) state the magnitude of the CO_2 flux to depend on several factors such as time since drying, temperature or state of the vegetation, which results in temporal fluctuations. Moreover, the spatial CO_2 distribution is likely to differ due to previously described heterogeneity and the influence of varying catchment characteristics including lithology, topography, soil types, climate and vegetation (Deirmendjian & Abril, 2018).

Due to the spatial and temporal dynamics that could not be covered within this study, the resulting distance proxy approach can consequentially only serve as first-order approximation and must be validated in future studies. Yet, given the complex nature and the large-scale system of the Elbe River, the presented methodological approach represents a straightforward mode for the upscaling of in situ CO_2 using spatial dependencies. As such, the entire approach may function as further refinement of CO_2 upscaling as presented, for example, in von Schiller et al. (2014). Assuming our study situation to be representative for the 117 days with comparable conditions (see Section 2.1), the approximate total CO_2 emission from exposed river sediments during the extreme 2018 drought amounts to ~6,200–6,600 t $year^{-1}$. Thus, the exposure of sediments created a considerable CO_2 source since the water of the Elbe River itself was undersaturated with respect to CO_2 (Staniek, 2019).

The upscaling of CO_2 emissions from exposed sediments to an entire river system as presented here combined with temporally continuous in-situ monitoring at various representative segments and locations along the river system may even provide the possibility to obtain temporally continuous CO_2 emission estimations on the large river system scale and thus a step forward compared with spatially and temporally discrete measurements. Herein, applied satellite products may be available every 2–5 days (Li & Roy, 2017), if no cloud interference is present. Radar remote sensing data, of the same Sentinel family for example, may provide earth information regardless of the cloud condition due to longer wavelengths that are not susceptible to atmospheric scattering. Thus, incorporating radar remote sensing to map water extents, as Bioresita, Puissant, Stumpf, and Malet (2018) have shown, facilitates the upscaling of in-situ CO_2 emissions to river system scale at a temporal resolution of less than 6 days. CO_2 emissions during droughts that may last in the order of days or weeks can thus be thoroughly estimated. The estimation may even be longterm since the Sentinel Mission is planned until 2030 with followup missions already planned beyond 2030 (Pahlevan, Sarkar, Franz, Balasubramanian, & He, 2017). Against the background of increased drought reoccurrence frequency in the future in the context of climate change (Stocker et al., 2013), the largescale monitoring option is especially important as consequentially the estimation would facilitate the monitoring of CO_2 emissions on a river scale and beyond over temporal scales relevant to climate change.

4 | CONCLUSIONS

The proposed methods facilitate the upscaling of spatially discrete CO_2 fluxes from exposed river sediments to the scale of an entire river. Through this upscaling, CO_2 fluxes can be quantified on larger and spatially continuous scales, providing an option to determine the effect of droughts on CO_2 fluxes. The option may become highly

relevant in light of an increased drought reoccurrence frequency in the future in the context of climate change.

The upscaling approach using detailed land cover even accounts for the natural spatial heterogeneity and may thus be preferable. Yet detailed land cover may not be generally available at other study sites or over larger spatial scales such as river systems. For these systems, water areas prior and during drought events, and thus exposed river sediment areas, can be easily extracted using different approaches and platforms (Ghahremani & Bondarev, 2017; Gleason et al., 2015; Kaplan & Avdan, 2017). This is why we argue that the corrected distance proxy is a reasonable and efficient approach to upscale discrete in-situ CO_2 measurements. However, as hydrogeological and sedimentological conditions may change along a river, distance dependency may be site specific and thus may vary from the 7 m distance value elaborated in the present study or even over time. However, both indicate a spatial heterogeneous flux attributable to the abiotic groundwater discharge along exposed river sediments and biotic mechanisms such as microbial activity and root respiration of pioneering plants.

For the Elbe River we derived values of 56.6 ± 64.8 tC day^{-1} (corrected distance proxy) and 52.9 ± 44.6 tC day^{-1} (land cover proxy) of CO_2 emissions from exposed river sediment during drought conditions. Both CO_2 emission values must be seen as first-order approximation since they represent temporally discrete measurements and are therefore representative for this moment in time only. Temporal dynamics such as vegetation development, temperature and drying effects and change of water level gradients will affect CO_2 emissions but could not be accounted for in this study. Consequentially, the dependency on temporal dynamics requires future research pursuing distance dependent long-term investigations to constrain the temporal variability of CO_2 flux of exposed river sediments. However, both approaches include the spatial heterogeneity of entire river systems. This inclusion is up to a level of detail that, given the complex nature of a large-scale river system, the approach may function as a further refinement for CO_2 upscaling compared with previous approaches.

Given a factually available high frequency satellite overpass of less than 6 days, the combination of the presented approach and temporally continuous in-situ CO_2 measurements, CO_2 emissions may be estimated quasi-continuous for entire river systems during droughts and beyond. Against the background of predicted increased drought reoccurrence frequency in the future in the context of climate change (Stocker et al., 2013), a river scale CO_2 monitoring would allow the estimation of CO_2 emissions on a regional scale and beyond over temporal scales relevant to climate change.

ACKNOWLEDGEMENTS

We thank Simon Kögler, Corinna Völkner and Dr. Max Köhne for help during field and lab measurements and Lutz Bannehr and his Gyrocopter team from the Hochschule Anhalt for performing flights. Gauge data of the Federal Waterways and Shipping Administration (WSV) were kindly provided by the German Federal Institute of Hydrology (BfG). We furthermore want to thank two anonymous reviewers for their careful reading, excellent comments and the time and effort both invested to improve the manuscript. This work was supported by funding from the Helmholtz Association in the framework of Modular Observation Solutions for Earth Systems (MOSES). The data that support the findings of this study are available from the corresponding author upon request. There are no conflicts of interest to declare.

ORCID

Ulf Mallast https://orcid.org/0000-0001-9238-3464
Matthias Koschorreck https://orcid.org/0000-0002-4393-3500

REFERENCES

Arce, M. I., MendozaLera, C., Almagro, M., Catalán, N., Romaní, A. M., Martí, E., … von Schiller, D. (2019). A conceptual framework for understanding the biogeochemistry of dry riverbeds through the lens of soil science. *EarthScience Reviews*, *188*, 441–453. https://doi.org/10.1016/j.earscirev.2018.12.001

Aubinet, M., Vesala, T., & Papale, D. (2012). *Eddy covariance: A practical guide to measurement and data analysis*. Dordrecht: Springer Science & Business Media. https://doi.org/10.1007/978-94-007-2351-1

Bannehr, L., Kirschke, T., Koppers, L., & Ulrich, C. (2015). Possible applications of a gyrocopter in the field of environmental research. Paper presented at the Digital Landscape Architecture 2015—Landscape Architecture and Planning, Dessau.

BfG. (2019). Das Niedrigwasser 2018. Koblenz: 22.

Bioresita, F., Puissant, A., Stumpf, A., & Malet, J. P. (2018). A method for automatic and rapid mapping of water surfaces from sentinel-1 imagery. *Remote Sensing*, *10*(2), 1–17. https://doi.org/10.3390/rs10020217

Bolpagni, R., Folegot, S., Laini, A., & Bartoli, M. (2017). Role of ephemeral vegetation of emerging river bottoms in modulating CO_2 exchanges across a temperate large lowland river stretch. *Aquatic Sciences*, *79*(1), 149–158. https://doi.org/10.1007/s00027-016-0486-z

Bolpagni, R., Laini, A., Mutti, T., Viaroli, P., & Bartoli, M. (2019). Connectivity and habitat typology drive CO_2 and CH_4 fluxes across land–water interfaces in lowland rivers. *Ecohydrology*, *12*(1), 1–12. https://doi.org/10.1002/eco.2036

Borken, W., Davidson, E. A., Savage, K., Gaudinski, J., & Trumbore, S. E. (2003). Drying and wetting effects on carbon dioxide release from organic horizons. *Soil Science Society of America Journal*, *67*(6), 1888–1896. https://doi.org/10.2136/sssaj2003.1888

Deirmendjian, L., & Abril, G. (2018). Carbon dioxide degassing at the groundwaterstreamatmosphere interface: Isotopic equilibration and hydrological mass balance in a sandy watershed. *Journal of Hydrology*, *558*, 129–143. https://doi.org/10.1016/j.jhydrol.2018.01.003

Drusch, M., Del Bello, U., Carlier, S., Colin, O., Fernandez, V., Gascon, F., … Martimort, P. (2012). Sentinel-2: ESA's optical highresolution mission for GMES operational services. *Remote Sensing of Environment*, *120*, 25–36. https://doi.org/10.1016/j.rse.2011.11.026

Du, Y., Zhang, Y., Ling, F., Wang, Q., Li, W., & Li, X. (2016). Water bodies' mapping from Sentinel-2 imagery with modified normalized difference water index at 10m spatial resolution produced by sharpening the SWIR band. *Remote Sensing*, *8*(4), 354. https://doi.org/10.3390/rs8040354

Duvert, C., Butman, D. E., Marx, A., Ribolzi, O., & Hutley, L. B. (2018). CO_2 evasion along streams driven by groundwater inputs and geomorphic controls. *Nature Geoscience*, *11*(11), 813–818. https://doi.org/10.1038/s41561-018-0245-y

Gallo, E. L., Lohse, K. A., Ferlin, C. M., Meixner, T., & Brooks, P. D. (2014). Physical and biological controls on trace gas fluxes in semiarid urban ephemeral waterways. *Biogeochemistry*, *121*(1), 189–207. https://doi.org/10.1007/s10533-013-9927-0

Ghahremani, A., & Bondarev, E. (2017). Water region extraction in thermal and RGB sequences using spatiotemporallyoriented energy features. *Electronic Imaging*, *2017*(13), 78–86. https://doi.org/10.2352/ISSN.2470-1173.2017.13.IPAS-205

Gleason, C., Smith, L., Finnegan, D., LeWinter, A., Pitcher, L., & Chu, V. (2015). Semiautomated effective width extraction from timelapse RGB imagery of a remote, braided Greenlandic river. *Hydrology and Earth System Sciences*, *19*(6), 2963–2969. https://doi.org/10.5194/hess-19-2963-2015

Gómez-Gener, L., Obrador, B., Marcé, R., Acuña, V., Catalán, N., CasasRuiz, J. P., … von Schiller, D. (2016). When water vanishes: Magnitude and regulation of carbon dioxide emissions from dry temporary streams. *Ecosystems*, *19*(4), 710–723. https://doi.org/10.1007/s10021-016-9963-4

Gómez-Gener, L., Obrador, B., von Schiller, D., Marcé, R., CasasRuiz, J. P., Proia, L., … Koschorreck, M. (2015). Hot spots for carbon emissions from Mediterranean fluvial networks during summer drought. *Biogeochemistry*, *125*(3), 409–426. https://doi.org/10.1007/s10533-015-0139-7

Hanson, P., Edwards, N., Garten, C. T., & Andrews, J. (2000). Separating root and soil microbial contributions to soil respiration: A review of methods and observations. *Biogeochemistry*, *48*(1), 115–146. https://doi.org/10.1023/A:1006244819642

Hensley, S., Zyl, J. V., Lavalle, M., Neumann, M., Michel, T., Muellerschoen, R., Pinto, N., Simard, M., & Moghaddam, M. (2015). Lband and Pband studies of vegetation at JPL. 2015 IEEE Radar Conference.

Humphries, P., & Baldwin, D. S. (2003). Drought and aquatic ecosystems: An introduction. *Freshwater Biology*, *48*(7), 1141–1146. https://doi.org/10.1046/j.1365-2427.2003.01092.x

Hutchinson, G., & Mosier, A. (1981). Improved soil cover method for field measurement of nitrous oxide fluxes 1. *Soil Science Society of America Journal*, *45*(2), 311–316. https://doi.org/10.2136/sssaj1981.03615995004500020017x

IKSE. (2005). Die Elbe und ihr Einzugsgebiet Ein geographischhydrologischer und wasserwirtschaftlicher Überblick I. K. z. S. d. Elbe: 262.

Jin, H., Yoon, T. K., Lee, S.H., Kang, H., Im, J., & Park, J.H. (2016). Enhanced greenhouse gas emission from exposed sediments along a hydroelectric reservoir during an extreme drought event. *Environmental Research Letters*, *11*(12), 124003. https://doi.org/10.1088/1748-9326/11/12/124003

Junk, W. J., Bayley, P. B., & Sparks, R. E. (1989). The flood pulse concept in riverfloodplain systems. *Canadian Special Publication of Fisheries and Aquatic Sciences*, *106*(1), 110–127.

Kaplan, G., & Avdan, U. (2017). Objectbased water body extraction model using Sentinel-2 satellite imagery. *European Journal of Remote Sensing*, *50*(1), 137–143. https://doi.org/10.1080/22797254.2017.1297540

Lake, P. S. (2003). Ecological effects of perturbation by drought in flowing waters. *Freshwater Biology*, *48*(7), 1161–1172. https://doi.org/10.1046/j.1365-2427.2003.01086.x

Lesmeister, L., & Koschorreck, M. (2017). A closedchamber method to measure greenhouse gas fluxes from dry aquatic sediments. *Atmospheric Measurement Techniques*, *10*(6), 2377–2382. https://doi.org/10.5194/amt-10-2377-2017

LHW. (2019). Flood warning system of the State of Saxony Anhalt.

Li, J., & Roy, D. P. (2017). A Global Analysis of Sentinel-2A, Sentinel-2B and Landsat8 Data Revisit Intervals and Implications for Terrestrial Monitoring. *Remote Sensing*, *9*(9), 902.

Light, T., Catalán, N., Giralt, S., & Marcé, R. (2019). CO2 and CH4 fluxes are decoupled from organic carbon loss in drying reservoir sediments. *Biogeosciences Discuss*. https://doi.org/10.5194/bg-2019-128

Looman, A., Maher, D. T., Pendall, E., Bass, A., & Santos, I. R. (2017). The carbon dioxide evasion cycle of an intermittent firstorder stream: Contrasting water–air and soil–air exchange. *Biogeochemistry*, *132*(1–2), 87–102. https://doi.org/10.1007/s10533-016-0289-2

Macklin, P. A., Maher, D. T., & Santos, I. R. (2014). Estuarine canal estate waters: Hotspots of CO_2 outgassing driven by enhanced groundwater discharge? *Marine Chemistry*, *167*, 82–92. https://doi.org/10.1016/j.marchem.2014.08.002

Marcé, R., Obrador, B., Gómez-Gener, L., Catalán, N., Koschorreck, M., Arce, M. I., … von Schiller, D. (2018). Emissions from dry inland waters are a blind spot in the global carbon cycle. *EarthScience Reviews*, *188*, 240–248.

Martinsen, K. T., Kragh, T., & SandJensen, K. (2019). Carbon dioxide fluxes of airexposed sediments and desiccating ponds. *Biogeochemistry*, *144*(2), 165–180. https://doi.org/10.1007/s10533-019-00579-0

McFeeters, S. K. (1996). The use of the Normalized Difference Water Index (NDWI) in the delineation of open water features. *International Journal of Remote Sensing*, *17*(7), 1425–1432. https://doi.org/10.1080/01431169608948714

Melack, J. M., Hess, L. L., Gastil, M., Forsberg, B. R., Hamilton, S. K., Lima, I. B., & Novo, E. M. (2004). Regionalization of methane emissions in the Amazon Basin with microwave remote sensing. *Global Change Biology*, *10*(5), 530–544. https://doi.org/10.1111/j.1365-2486.2004.00763.x

Mertes, L. A. (2002). Remote sensing of riverine landscapes. *Freshwater Biology*, *47*(4), 799–816. https://doi.org/10.1046/j.1365-2427.2002.00909.x

Mishra, A. K., & Singh, V. P. (2010). A review of drought concepts. *Journal of Hydrology*, *391*(1–2), 202–216. https://doi.org/10.1016/j.jhydrol.2010.07.012

Otsu, N. (1979). A threshold selection method from graylevel histograms. *IEEE Transactions on Systems, Man, and Cybernetics*, *9*(1), 62–66. https://doi.org/10.1109/TSMC.1979.4310076

Pahlevan, N., Sarkar, S., Franz, B., Balasubramanian, S., & He, J. (2017). Sentinel-2 MultiSpectral Instrument (MSI) data processing for aquatic science applications: Demonstrations and validations. *Remote Sensing of Environment*, *201*, 47–56. https://doi.org/10.1016/j.rse.2017.08.033

Peters, E., Bier, G., Van Lanen, H., & Torfs, P. (2006). Propagation and spatial distribution of drought in a groundwater catchment. *Journal of Hydrology*, *321*(1–4), 257–275. https://doi.org/10.1016/j.jhydrol.2005.08.004

Pumpanen, J., Kolari, P., Ilvesniemi, H., Minkkinen, K., Vesala, T., Niinistö, S., … Pihlatie, M. (2004). Comparison of different chamber techniques for measuring soil CO_2 efflux. *Agricultural and Forest Meteorology*, *123*(3–4), 159–176. https://doi.org/10.1016/j.agrformet.2003.12.001

Rogers, J. N., Parrish, C. E., Ward, L. G., & Burdick, D. M. (2018). Improving salt marsh digital elevation model accuracy with fullwaveform lidar and nonparametric predictive modeling. *Estuarine, Coastal and Shelf Science*, *202*, 193–211. https://doi.org/10.1016/j.ecss.2017.11.034

Roth, K., Schulin, R., Flühler, H., & Attinger, W. (1990). Calibration of time domain reflectometry for water content measurement using a composite dielectric approach. *Water Resources Research*, *26*(10), 2267–2273.

Scholten, M., Anlauf, A., Büchele, B., Faulhaber, P., Henle, K., Kofalk, S., … Rast, G. (2003). The River Elbe in Germanypresent state, conflicting goals, and perspectives of rehabilitation. *Large Rivers*, *15*, 579–602. https://doi.org/10.1127/lr/15/2003/579

Scholz, M. (2005). *Lebensräume der Elbe und ihrer Auen*. Berlin: Weißensee Verlag.

Staniek, M. (2019). Distribution of greenhouse gas concentrations along two characteristic Elbe segments. BSc Bachelor Thesis, MartinLuther University HalleSaale.

Steward, A. L., von Schiller, D., Tockner, K., Marshall, J. C., & Bunn, S. E. (2012). When the river runs dry: human and ecological values of dry

riverbeds. *Frontiers in Ecology and the Environment*, *10*(4), 202–209. https://doi.org/10.1890/110136

Stocker, T. F., Qin, D., Plattner, G.K., Tignor, M., Allen, S. K., Boschung, J., … Midgley, P. M. (2013). *Climate change 2013: The physical science basis*. Cambridge: Cambridge University Press.

Striegl, R. G., Dornblaser, M. M., McDonald, C. P., Rover, J. R., & Stets, E. G. (2012). Carbon dioxide and methane emissions from the Yukon River system. *Global Biogeochemical Cycles*, *26*(4). https://doi.org/10.1029/2012GB004306

Tweed, S., Leblanc, M., & Cartwright, I. (2009). Groundwater–surface water interaction and the impact of a multiyear drought on lakes conditions in SouthEast Australia. *Journal of Hydrology*, *379*(1–2), 41–53. https://doi.org/10.1016/j.jhydrol.2009.09.043

Van Niel, T. G., McVicar, T. R., & Datt, B. (2005). On the relationship between training sample size and data dimensionality: Monte Carlo analysis of broadband multitemporal classification. *Remote Sensing of Environment*, *98*(4), 468–480.

von Schiller, D., Marcé, R., Obrador, B., Gómez-Gener, L., CasasRuiz, J. P., Acuña, V., & Koschorreck, M. (2014). Carbon dioxide emissions from dry watercourses. *Inland Waters*, *4*(4), 377–382. https://doi.org/10.5268/IW-4.4.746

Watanabe, Y., & Kawahara, Y. (2016). UAV photogrammetry for monitoring changes in river topography and vegetation. *Procedia Engineering*, *154*, 317–325. https://doi.org/10.1016/j.proeng.2016.07.482

Weise, L., Ulrich, A., Moreano, M., Gessler, A., Kayler, Z. E., Steger, K., … Premke, K. (2016). Water level changes affect carbon turnover and microbial community composition in lake sediments. *FEMS Microbiology Ecology*, *92*(5), fiw035. https://doi.org/10.1093/femsec/fiw035

SUPPORTING INFORMATION

Additional supporting information may be found online in the Supporting Information section at the end of this article.

How to cite this article: Mallast U, Staniek M, Koschorreck M. Spatial upscaling of CO_2 emissions from exposed river sediments of the Elbe River during an extreme drought. *Ecohydrology*. 2020;13:e2216. https://doi.org/10.1002/eco.2216